# Optical and electrical investigation of plasma generated by high-energy self-stabilized spark ignition system

Mário Janda ✉ ; Kostyantyn Korytchenko; Olga Shypul; ... et. al

Check for updates

CrossMark

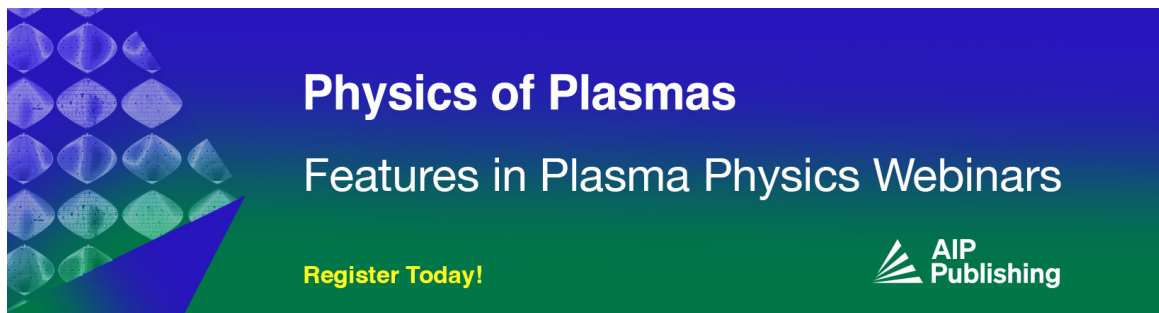View Online    Export Citation

**Physics of Plasmas**

Features in Plasma Physics Webinars

Register Today!

AIP Publishing

AIP Publishing

# Optical and electrical investigation of plasma generated by high-energy self-stabilized spark ignition system

View Online   Export Citation   CrossMark

Mário Janda,[1,a] (iD) Kostyantyn Korytchenko,[2] (iD) Olga Shypul,[3] (iD) Serhiy Krivosheev,[2] (iD) Oleksandr Yeresko,[2]
and Anatoly Kasimov[2] (iD)

## AFFILIATIONS

[1]Faculty of Mathematics, Physics and Informatics, Comenius University, Mlynska dolina, 84248 Bratislava, Slovakia
[2]National Technical University "Kharkiv Polytechnic Institute," 2 Kirpichova Str., 61002 Kharkiv, Ukraine
[3]National Aerospace University "Kharkiv Aviation Institute," 17 Chkalova Str., 61070 Kharkiv, Ukraine

[a]Author to whom correspondence should be addressed: mario.janda@fmph.uniba.sk

## ABSTRACT

Spark discharge plasma is commonly used for ignition in internal combustion engines. The environmental performance of internal combustion engines with forced ignition is improved when operating under lean mixture conditions. High-energy ignition systems are needed to ensure reliable ignition of lean mixtures. The ignition of a combustible mixture is influenced by several plasma parameters, such as the temperature of its various components, the size of the plasma, and the deposited energy. It is, therefore, beneficial to know these parameters. Here, we present optical and electrical investigation of plasma generated in ambient air by a novel high-energy self-stabilized spark ignition system. The electrical investigation showed two high current pulses, with the current amplitude of ∼40 and ∼150 A. The energy is deposited to the spark gap mainly during the second current pulse, and it is increasing from 213 to 541 mJ with the increasing gap size from 3 to 13 mm. The energy efficiency increases with the gap as well, from around 23% to 58%. Time-resolved emission spectra enabled us to estimate the evolution of the gas temperature, electron excitation temperature, and electron density in the generated plasma. It was found that the highest electron density, $3–4 \times 10^{17} \, \text{cm}^{-3}$, correlates with the maximum of the second pulse current. We observed a specific plasma evolution between the two current pulses, with an increase in temperature from 4500 to 7500 K and a contraction of the plasma channel diameter from 3.3 to 0.5 mm.

## I. INTRODUCTION

Gas plasmas generated by electrical discharges have found wide application in biomedicine, pollution control, or agriculture, where various media or surfaces are treated.[1–3] In these applications, non-equilibrium plasma is more commonly used, in order to avoid gas heating and for low power consumption. Thermal equilibrium plasma, generated, for example, by arc discharges, can also be used in various applications. High-energy costs allow their utilization only for applications where one can either expect valuable products (e.g., $H_2$) or needs to completely destroy very dangerous pollutants.[4–6] Pulsed arc discharges, or spark discharges, in which the transition from non-equilibrium to partially equilibrium plasma develops are also of potential interest for the use for thermal decomposition of various media, or generation of nanoparticles.[7]

More commonly, spark discharges are used for ignition in internal combustion engines. Despite the tendency to switch to electric engines in cars, different types of internal combustion engines will be still used for at least several decades. It is, therefore, desirable to develop new more environmentally friendly advanced ignition systems, using, for example, alternative fuels.[8] The environmental performance of internal combustion engines with forced ignition is better when they operate under lean mixture conditions.[9]

Reliable ignition of lean mixtures requires higher energy ignition systems because the minimum ignition energy increases with increasing air/fuel ratio.[10] High-energy ignition systems are also used for cold start of diesel engines, to ignite fuel oil in boilers, or to ignite gas turbines.[11] At the same time, advanced ignition systems are required to ensure reliable ignition of the combustible mixture in a high-speed gas

flow because an increase in flow velocity necessitates a higher minimum ignition energy.[12] Finally, it is also desirable to increase the energy efficiency of ignition systems because the energy efficiency of typical automotive ignition system is below 1%.[13]

To improve ignition reliability and increase the energy efficiency of ignition systems, it is important to understand the characteristics of the generated plasma. The plasma parameters, such as the temperature evolution of its various components and the size of the plasma, affect the combustible mixture ignition, especially under lean mixture and/ or high gas flow conditions.

In the present work, the results of the electrical and optical diagnostics of an improved high-energy ignition system are given. Improvement of this ignition system is aimed at improving the reliability of ignition of the combustible mixture under the conditions of exposure to a high-speed gas flow directed perpendicular to the discharge channel. The electric circuit used is not completely new,[14,15] but it was improved by including an additional switch that makes it possible to provide self-stabilization of the discharge under the influence of a high-speed gas flow having impact on the stability of the generated plasma channel.[16] The increasing air velocity extends the plasma channel length. Thus, if a constant voltage source is connected to the channel, the electric field strength in the plasma channel decreases. Finally, this would lead to interruption of the discharge current. Thus, further deposition of energy needed for the ignition is not possible. In the presented electrical circuit, however, the increasing length and the increasing resistance of the plasma channel cause an increase in self-induced electromotive force in the circuit. As a result, the voltage across the spark gap increases, eliminating the interruption of the discharge current.

Earlier, we conducted a photographic study of the ignition area,[17] and the influence of the high-speed gas flow on the discharge development in the ignition system was under consideration.[16] The present work is a continuation of previous studies. Detailed electrical characteristics, energy deposition efficiency, and several plasma characteristics obtained by optical emission spectroscopy (OES) are presented. The OES technique can provide valuable information on excited atomic and molecular states. It enables us to determine the rotational, vibrational, and electronic excitation temperatures of the plasma and, thus, the level of non-equilibrium and the gas temperature.[18,19]

Knowing these plasma parameters is important for future optimization of the ignition. The kinetic temperature of molecules and atoms must exceed the ignition temperature of a combustible mixture, but it is desirable not to waste too much energy for thermal dissociation and ionization of molecules. It is, therefore, preferable to use non-equilibrium plasma for energy-efficient high-energy ignition, with sufficient kinetic temperature of the heavy particles (above the ignition temperature), but even higher temperature of electrons. High-energy electrons can efficiently generate reactive chemical species, enhancing the combustion chemistry. For this purpose, non-equilibrium plasma is also used for a stabilization of lean flames.[20,21]

The electron density $n_e$, which is one of the crucial parameters for the assessment of the plasma characteristics, can be also determined by optical emission spectroscopy. The most common OES method for $n_e$ measurement is based on the Stark broadening of atomic emission lines, and the Stark broadening of tens of lines of many species has already been studied.[22,23] In the present work, we also determined density of electrons in generated plasma based on

Stark broadening of Hα line and atomic oxygen O triplet line near 777 nm.

Time-resolved evolution of plasma channel diameter obtained by imaging technique is also presented. The knowledge of deposited energy, temperature, and the plasma dimensions is useful to estimate whether a critical size of sufficiently hot plasma is generated for reliable ignition. Next, data obtained by OES technique are also useful as input for future numerical modeling of plasma generated by the presented ignition system.

## II. EXPERIMENTAL SETUP

Here, we will first describe the operation principles of a high-energy self-stabilized spark ignition system (Subsec. II A). Next, we will describe the experimental setup and methodology used for electrical (Subsec. II B 1) and optical (Subsec. II B 2) diagnostics of the presented ignition system.

### A. Design and operation of the advanced high-energy ignition system

Figure 1 shows a schematic electrical circuit of the studied high-energy self-stabilized spark ignition system. This circuit is not completely new,[14,15] but it was improved by including the switch $S_2$ in parallel with the capacitor $C_2$. Adding the switch $S_2$ makes it possible to provide self-stabilization of the discharge under the influence of a high-speed gas flow influencing the stability of generated plasma channel.

Initially, capacitors $C_1$ and $C_2$ are charged from external voltage sources, which are not shown in the diagram. Next, the switch $S_1$ is closed, which leads to the supply of a voltage pulse to the primary winding of the step-up transformer $T_1$. This leads to the appearance of a high-voltage pulse on the secondary winding of the transformer, causing gas breakdown in the gap and appearance of the initial spark current pulse.

After the gap is bridged by a highly conductive plasma channel, the discharging of the capacitor $C_2$ through the secondary winding of the transformer $T_1$ and through the plasma channel begins. A transient response of a series RLC-circuit with the capacitor $C_2$ starts. This would lead to damped sinusoidal current oscillations, if switch $S_2$ remains opened. However, the switch $S_2$ is closed when the current in the circuit reaches its maximum value, and the voltage across the capacitor drops to zero. The closing time $t$, thus, corresponds to the first 1/4 of the current oscillation cycle ($t = 1/4T$).
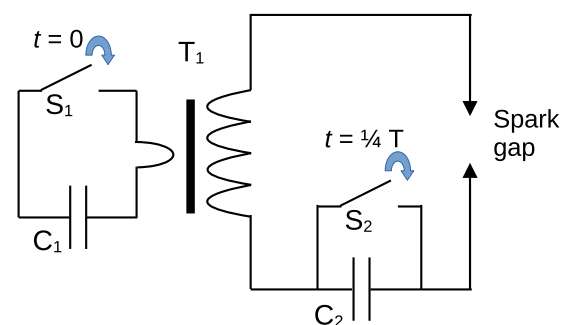


**FIG. 1.** Schematic diagram of the developed ignition system.

Before the switch $S_2$ closes, the energy of the magnetic field is accumulated in the inductance of the transformer winding. When the switch $S_2$ is closed, the RLC-circuit oscillations are interrupted, but further flow of the spark discharge is ensured by the release of the energy accumulated in the secondary winding of the transformer. This leads to the formation of the second discharge current pulse. The characterization of discharge current during this phase is one of the goals of this work.

## B. Methodology

Figure 2 shows a schematic diagram of the experimental apparatus used for electrical and optical diagnostics of the studied high-energy self-stabilized spark ignition system.

### 1. Measurement of the electrical parameters

The study of the electrical parameters of the developed ignition system was carried out using two different setups. In one set of experiments, the spark discharge current was measured by a Pearson Electronics 2877 (1 V/A) current transformer with a response time of around 1 ns (Fig. 2). Voltage probes Tektronix P6015A was used to measure the discharge voltage. Both electrical signals were registered by the Tektronix TBS2104 oscilloscope. The length of the spark gap was 3 mm when using this setup.

In the second set of experiments, the length of the spark gap varied from 0.5 to 13 mm. Current was measured by a CSNM191 Honeywell current sensor with a measurement error of $\pm0.5\%$ and a response time of less than 1 $\mu$s. The sensitivity of the CSNM191 sensor after converting the current signal into a voltage signal was $100 \pm 0.51$ A/V. In this second setup, the voltage probe HVP-39pro PINTEK was used to measure the voltage, and both electrical signals were registered by a Rigol DS1104 oscilloscope. The measurement error of the HVP-39pro probe is 3% of full scale. Due to the relatively high-voltage measurement error of this probe, the capacitor charge voltage was also measured with a UNI-T UT-58C multimeter with a measurement error of $\pm0.5\%$ in the measurement range under study. The capacitance of capacitors was measured using an E7–22 RLC meter with a measurement error of $\pm0.009$ $\mu$F.
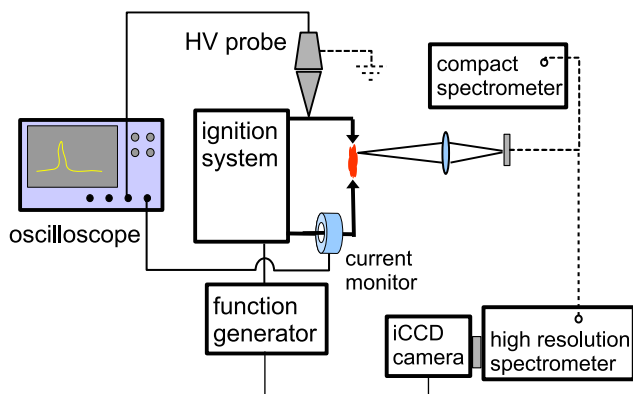


**FIG. 2.** Schematic diagram of the experimental setup used for electrical and optical diagnostics of the developed ignition system.

### 2. Optical diagnostic techniques

Two different devices were used for optical diagnostics of generated plasma: a compact optical emission spectrometer and a high resolution spectrometer coupled with a fast intensified CCD camera. The length of the spark gap was 3 mm during experiments focused on the optical diagnostics. The experiments were carried out using a copper cathode and an aluminum anode. These materials are not typically used at the spark plugs due to high sputtering. We used these materials instead of more commonly stainless steel to simplify the OES measurements. According to the NIST database,[24] Al, $Al^+$, Cu, and $Cu^+$ combined have only 574 spectral lines in the range 200–900 nm with observed wavelengths, and with Einstein's coefficient for the spontaneous emission (transition strength) above $10^6$ $s^{-1}$. In the case of Fe and $Fe^+$, there are 5138 lines that fulfill these criteria.

The compact emission spectrometer Avantes AvaSpec-Mini4096CL (200–1100 nm, resolution 0.5–0.7 nm) was used for fast recording of the time-integrated spectra of a broad spectral region. The time-resolved emission spectra with high spectral resolution were obtained using the 2 m spectrometer Carl Zeiss Jena PGS2, coupled with an intensified CCD camera (Andor Istar) with a 2 ns minimum exposure time. The iCCD camera was synchronized with the studied ignition system by a function generator Tektronix AFG2021. This generator triggered both the ignition system and the CCD camera by transistor–transistor logic (TTL) compatible 5 V pulses with a frequency of 10 Hz.

The adjustable entrance slit enabled us to use the intensified CCD camera either for imaging of the plasma channel (with entrance slit fully opened to 300 $\mu$m) or for spectroscopic measurements (slit 50–100 $\mu$m and spectral resolution 0.05–0.09 nm). The relatively fine spectral resolution of our spectrometer enables us to observe the broadening of atomic and ionic lines caused by free electrons in the plasma, the Stark effect. The measurement of the emission lines' Stark broadening is the most common OES method for the calculation of the electron density $n_e$ in atmospheric pressure plasmas, and the Stark broadening of tens of lines of many species has already been studied.[22,23] In the present work, we determined the density of electrons in the generated plasma based on Stark broadening of the H$\alpha$ line and atomic oxygen O triplet line near 777 nm.

Hydrogen-like and helium-like lines are the most sensitive to Stark broadening, and they are the most commonly used for the determination of electron density in the plasma. The difficulty with the Stark broadening of the H$\alpha$ line is that it depends not only on $n_e$ but also on electron temperature $T_e$ and ion dynamics. In order to avoid problems with the dependence of the full width at the half maximum (FWHM) of the Stark broadened H$\alpha$ line on $T_e$, we calculated $n_e$ from the H$\alpha$ line the full width at the half area (FWHA), using the formula derived by Gigosos et al.,[25]

$$\Delta\lambda_{FWHA}^{H\alpha} = 0.549\text{nm} \times \left(\frac{n_e}{10^{23}\,\text{m}^{-3}}\right)^{0.67965}. \quad (1)$$

Here, $\Delta\lambda_{FWHA}^{H\alpha}$ is the FWHA of the H$\alpha$ line in nm. This formula covers the range of electron densities between $10^{14}$ and $10^{19}$ $cm^{-3}$ and of electron temperatures between 1000 and 175 000 K.

Stark broadening of the O triplet ($^5S^o$, J = 2 $\rightarrow$ $^5P$, and J = 1–3) near 777 nm does not significantly depend on $T_e$. However, a disadvantage results from the overlapping of the three lines of the triplet at higher electron densities. The Stark broadening of this line is included

in the Specair software.[18,26] We, therefore, used Specair to fit the experimental spectra to get $n_e$ by changing the gas temperature, pressure, and the molar fraction of the electrons. The advantage of using Specair is that simulated spectra can be convoluted with the measured instrumental broadening function. Doppler and collisional Van der Waals broadening are also included. Indeed, spectra have to be simulated under conditions relevant to experimentally measured spectra.

The kinetic temperature of the heavy particles needed to estimate the Doppler broadening can be approximated in atmospheric pressure air plasmas by rotational temperature $T_r$ of $N_2(C^3\Pi_u)$ species.[18] The rotational temperature of $N_2(C^3\Pi_u)$ can be obtained by fitting the experimental spectra of the molecular nitrogen second positive emission system (SPS), corresponding to the transition from state $N_2(C^3\Pi_u)$ to state $N_2(B^3\Sigma_g)$. For this purpose, we used synthetic spectra generated by the Specair software.[18,26]

The temperature of electrons can be approximated by the electron excitation temperature obtained by fitting of emission spectra of several atomic or ionic lines. For this purpose, we used our own program. The experimental spectra were compared with synthetic spectra of N, O, $Cu^+$, Al, and $Al^+$, generated at different electron excitation temperatures ($T_{exc}$), taking into account the broadening processes (instrumental broadening of our spectrometer, Doppler broadening, and collisional broadening).

## III. RESULTS AND DISCUSSION

First, the electrical characteristics of the used electrical circuit were determined. It was found out that the capacitance of the capacitor $C_1$ is $8.005 \pm 0.009\,\mu F$, and the capacitance of the capacitor $C_2$ is $2.708 \pm 0.009\,\mu F$, at a measurement frequency of 1 kHz. The initial charging voltage of both capacitors was $828 \pm 6$ V, since the charge was carried out from the same voltage source. The capacitance of the capacitor $C_2$ is the important parameter determining the amount of available energy that can be deposited to the spark gap.

Next, the resistance of the transformer secondary winding and the resistance of connecting wires were determined according to Ohm's law, by measuring the secondary winding voltage and the direct current flowing through the winding from a direct current source. It was found that the total resistance of winding and connecting wires is equal to $R_{wire} = 0.180 \pm 0.05\,\Omega$. The internal resistance of the capacitor $C_2$, $R_{cap}$, was measured as well. It is equal to $0.04\,\Omega$.

Only after these preparatory measurements, discharge generated by the presented high-energy spark ignition system was studied. The obtained results from the electrical and the optical measurements are complementary, and there is direct correlation of the optical and the electrical signals. However, for easier understanding of the optical data, we start with the description of the electrical characteristics of generated discharge in Subsec. III A. Obtained results enabled us to calculate the energy deposited to the spark gap, described in Subsec. III B. The description of plasma characteristics derived from optical measurements follows in Subsec. III C.

### A. Electrical characteristics of the generated discharge

Figure 3 shows voltage and current waveforms characteristic for the presented ignition system. There are two major current pulses. The first current pulse, with the amplitude above 40 A (time interval 0–0.3 $\mu$s on Fig. 3, black dashed line), was measured by the Pearson current monitor. An oscillatory-damping of the discharge current
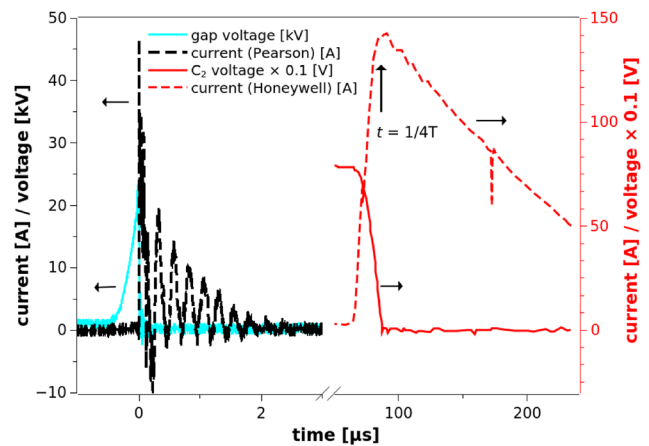


**FIG. 3.** Measured voltage and current waveforms; voltage across the spark gap (cyan solid line), current measured by Pearson current monitor (black dashed line), current measured by Honeywell current sensor (red dashed line), and voltage $u_{C2}$ across the capacitor $C_2 \times 0.1$ (solid red line).

occurs in the circuit after the first current pulse, with a main oscillation frequency of about 3.3 MHz (time 0.3–2 $\mu$s on Fig. 3). Oscillations with this frequency and negative current component are possible due to the presence of parasitic capacitances formed between the turns of the secondary winding of the transformer, decreasing the inductance of the circuit.

A second current pulse with the amplitude above 135 A appears much later, with a delay around 80 $\mu$s. The second current pulse was measured by the CSNM191 Honeywell current sensor. It is necessary to combine these two devices to see the current evolution in the circuit correctly because the core of the Pearson current monitor becomes saturated during the second current peak, and the CSNM191 current sensor is not fast enough to record correctly the first current pulse.

The first current pulse is a consequence of a high-voltage pulse across the spark gap with the peak voltage >20 kV, formed after the switch $S_1$ is closed (time interval −0.5 to 0 $\mu$s on Fig. 3). The rise time of the high voltage (HV) pulse is below 0.5 $\mu$s. The strong electric field in the gap during the HV pulse causes the gas breakdown and the formation of the spark current pulse. The gas breakdown in atmospheric pressure air takes place by a streamer mechanism.[27–29] This mechanism is still studied experimentally and can be described as two peak processes[30,31] because the spark (breakdown) current pulse is preceded by a smaller streamer current pulse, with typical amplitude in order of 10 mA.

In contrast to a typical spark discharge, the discharge generated by the presented ignition system should be described as a three peak process, with streamer current pulse, the breakdown spark current pulse, and the second post-breakdown current pulse (time interval 80–240 $\mu$s on Fig. 3, red dashed line). Streamer, however, is not detectable by our probes, and it has no direct impact on the ignition. Henceforth, we shall, therefore, deal only with the two later pulses, describing them for simplicity as the first, and as the second current pulse.

The second current pulse formed by discharging of the capacitor $C_2$ is a specific feature of the presented ignition system discharge circuit. The delay between the two current pulses is typically in the range from 60 to 125 $\mu$s. The presence of the delay between the gas

breakdown (the first spark current pulse) and the second current pulse can be explained by a high reactance of the secondary winding of the transformer. However, as the current in the circuit gradually increases in time after the first current pulse up to $3 \pm 1$ A, the saturation of the transformer core is reached, and its reactance decreases. The decrease in reactance enables fast discharging of the capacitor $C_2$ and the second current pulse formation.

When the current during the second pulse reaches the peak value, the voltage across the capacitor $C_2$, $u_{C2}$, decreases to 0 (Fig. 3, red solid line, time $\sim 90$ $\mu s$). If switch $S_2$ remains opened, damped sinusoidal current oscillations characteristic for the RLC circuits would follow. Since the switch $S_2$ is closed when the current reaches its maximum value and $u_{C2}$ drops to zero, further discharging of the capacitor $C_2$ does not occur. The further flow of the discharge current is caused by the process of releasing the magnetic field energy accumulated in the inductance of the transformer's secondary winding. As a result, the measured current after the moment when $S_2$ is closed corresponds to the transient in a RL circuit.

Figure 4 shows comparison of the second current pulses measured at two different lengths of the gap. The increasing gap size leads to a decrease in the amplitude and the duration of the second current pulse. These differences can be explained by the influence of the circuit resistance in the RL-circuit on the second current pulse. The resistance of the winding and the resistance of the connecting wires do not change, but the total resistance of the circuit includes also the resistance of the generated plasma channel. As the distance between the electrodes increases, the resistance of the plasma channel also increases. The increase in the total resistance of the RL-circuit can explain the decrease in the amplitude and in the duration of the second current pulse with the increasing gap length.

The increasing spark channel resistance with the growing gap size can explain also the prolongation of the delay between the first and the second current pulse. The delay increases approximately linearly from $60 \pm 5$ $\mu s$ at gap size 0.5 mm, up to around $125 \pm 5$ $\mu s$ at gap size 13 mm. The prolonging delay is associated with slower increase in the discharge current after the first current pulse, when the



**FIG. 4.** Comparison of discharge currents obtained at spark gap lengths of 0.5 and 13 mm.

circuit reactance is larger. Consequently, the time needed to achieve the transformer core saturation increases.

## B. Calculation of the energy deposited to plasma

The resistance of the plasma channel mentioned earlier is important factor influencing the amount of energy deposited to the gas. The deposited energy, in turn, is a crucial parameter influencing the ignition of combustible mixtures. First, let us consider the energy input corresponding to the first current pulse. The upper limit of available energy that could be deposited to the plasma during the first current pulse can be obtained by calculating the energy $Q_1$ released during the discharging of the capacitor $C_1$ on the primary winding of the transformer,

$$Q_1 = \frac{1}{2} C_1 \left( u_{c1}^2(0) - u_{c1}^2(t_1) \right). \quad (2)$$

Here, $t_1$ is the duration of the discharging period during which the switch $S_1$ is closed, $u_{c1}(0)$ is the voltage across the capacitor $C_1$ at the beginning of the discharging (828 V), and $u_{c1}(t_1)$ is the voltage across the capacitor $C_1$ at time $t_1$. The difference between $u_{c1}(0)$ and $u_{c1}(t_1)$, $\Delta u$, can be calculated by following equation:

$$\Delta u = \frac{1}{C_1} \int_0^{t_1} i_1 dt, \quad (3)$$

where $i_1$ is an average current in the primary circuit. Using $t_1 = 1$ $\mu s$ and $i_1 = 200$ A, as measured by a current sensor located in the branch with the capacitor $C_1$, we obtain the voltage drop $\Delta u = 25$ V. Thus, the total energy that could be deposited to the gap during the first current pulse does not exceed 163 mJ. The real value is certainly much lower, if we take into the account the low efficiency of conversion of the energy released during the discharging of the capacitor $C_1$ on the primary winding of the transformer into the energy released in the spark gap. As a rule of thumb, the conversion efficiency is much lower than 50%.[32]

More energy that could be deposited to the gap is available during the second current pulse. The analysis of electrical circuit enabled us to develop computational technique to calculate time evolution of the total amount of available energy, $Q_{total}(t)$, in our system,[33] defined by the equation

$$Q_{total}(\tau) = \int_{t_2}^{\tau} R_{total}(t) i^2(t) dt. \quad (4)$$

Here, $t_2$ indicates the beginning of the second current pulse and $R_{total}(t)$ is the time variable total resistance of the circuit. $R_{total}(t)$ was obtained by solving the following equation:

$$L \frac{di}{dt} + i . R_{total} + u_{C2} = 0, \quad \text{with } u_{C2} = 0 \text{ for } t > 1/4T. \quad (5)$$

Here, $L$ is the circuit inductance during the second current pulse when the transformer core is saturated, and $i$ and $u_{C2}$ are experimentally measured discharge current and the voltage across capacitor $C_2$.

The final value of $Q_{total}$, for $\tau \to \infty$, can be more easily calculated using following formula:
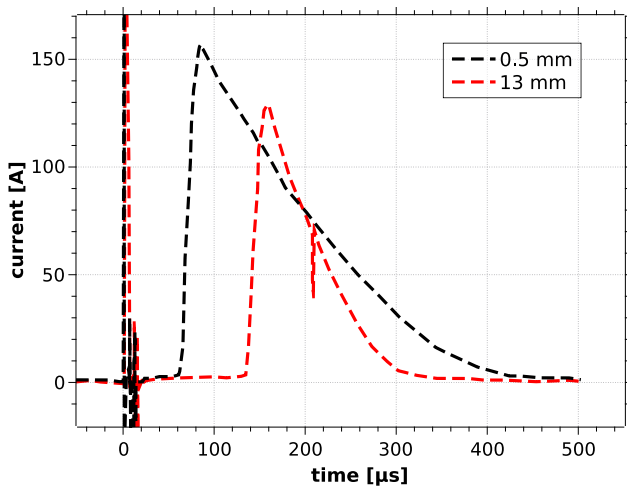
$$Q_{total}(\infty) = \frac{1}{2} C_2 u_{C2}^2, \quad (6)$$

assuming that the voltage across capacitor C$_2$ drops to zero during the second current pulse (Fig. 3). With initial voltage 828 V and capacity 2.7 μF, we obtain $Q_{total}(\infty) = 928$ mJ. It is advantageous, however, to use Eqs. (3) and (4) to calculate $Q_{total}(t)$ as a function of time because it enables us to estimate the energy deposited to the spark gap.

The true amount of energy deposited to the spark gap which could be used to ignite combustible mixtures, $Q_{ign}$, is lower than the total available energy. $Q_{ign}$ can be estimated from $Q_{total}$ after deduction of energy losses,

$$Q_{ign}(\tau) = Q_{total}(\tau) - Q_{el}(\tau) - \int_{t_2}^{\tau} (R_{wire} + R_{cap}) i^2(t) dt. \quad (7)$$

Here, $R_{wire}$ is the wire resistance, $R_{cap}$ is the internal resistance of the capacitor C$_2$, and $Q_{el}$ is losses due to energy deposited to electrodes, causing their sputtering. It is possible to estimate $Q_{el}$ by the expression

$$Q_{el}(\tau) = \int_{t_2}^{\tau} u_{el} i(t) dt, \quad (8)$$

where $u_{el}$ is the voltage drop across the electrodes during the current pulse. The experiments were carried out using a copper cathode and an aluminum anode. According to the reference data,[34] the voltage drop across the electrodes for an arc discharge with current $i = 20$–200 A is in the range of 18–22 V.

Figure 5 shows time evolution of $Q_{ign}$ and $Q_{el}$ calculated from measured current profiles for two different gaps, 3 and 13 mm, using $u_{el} = 20$ V. Time t = 0 μs on this figure represents the beginning of the second current pulse. As we can see, the final value of $Q_{ign}$, for t → ∞, is higher in 13 mm gap than in 3 mm gap. Knowing $Q_{ign}$ is important because it affects the combustible mixture ignition reliability. Moreover, the time evolution of $Q_{ign}$ enables us to estimate the rate of energy deposition. Higher rate of deposition, resulting in a stronger shock wave, would be favorable for a detonation, not for the deflagration ignition process. Reasonable rate of energy deposition with less energy spent for shock wave is more suitable for the energy-efficient ignition of combustible mixtures.
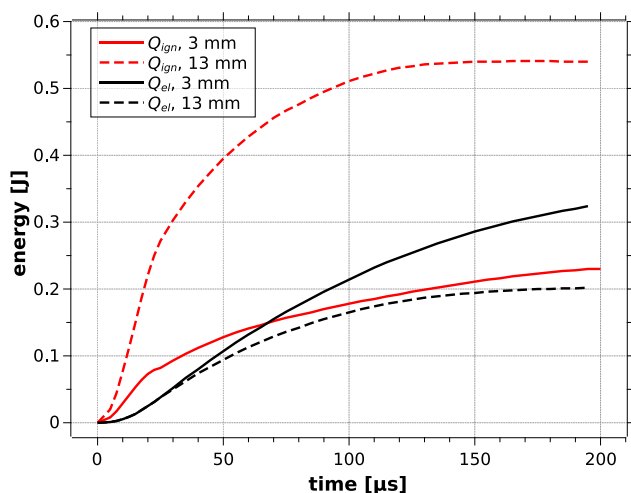
Figure 6 shows dependence of $Q_{ign}(\infty)$ on the gap size, calculated from measured current profiles, using $u_{el} = 20$ V. We see monotonous increase in $Q_{ign}(\infty)$ from 0.23 to 0.54 J with the increasing gap size from 3 to 13 mm. It is interesting to compare these values with a typical minimum ignition energy. The minimum ignition energy depends on the equivalence ratio and turbulent intensities in the combustible gases.[35] In lean methane-air mixtures with the equivalence ratio of 0.6 and normalized turbulent intensity around 300, the minimum ignition energy exceeds 0.1 J.[35] In our system, $Q_{ign}(\infty)$ is always higher than 0.1 J.

Because $Q_{ing}(\infty)$ increases with the spark gap size, the energy deposition efficiency, defined as $\eta_{ign} = 100 \times Q_{ign}(\infty)/Q_{total}(\infty)$, must increase with gap size as well (Fig. 6, red squares). The efficiency of typical automotive ignition system is significantly less than 1%.[13] Here, the energy efficiency increases from 23% to 58% with the gap increasing from 3 to 13 mm. The increase in the energy efficiency deposition with the increasing spark channel length can explain the stability of presented ignition system under high gas flow conditions.[16] In other ignition systems, high gas flow can distort the spark channel and reduce the deposited energy.[36]

We assume that with the energy efficiency up to 58%, the presented ignition systems will be suitable for reliable and energy-efficient ignition of lean mixtures, which are hard to ignite. It is necessary to emphasize, however, that the achieved energy efficiency characterizes the presented ignition system only and is not to be confused with an overall performance of a combustion engine where it would be used.

The increase in $Q_{ign}(\infty)$ and $\eta_{ign}$ can be explained by increasing resistance of the generated spark plasma channel, $R_{plasma}$, with the growing gap size. The plasma channel resistance can be approximated by the total resistance of the circuit, $R_{total}$, calculated by solving Eq. (5), after the deduction of $R_{wire}$ and $R_{cap}$.

Figure 7 shows time evolution of $R_{plasma}$ for two different spark gaps, where t = 0 μs represents the time when the peak current was achieved during the second current pulse. Comparing the plasma resistance for 0.5 mm gap and 13 mm gap, we can see that the minimal plasma resistance (in t = 0 μs) is lower in 0.5 mm gap. Next, the $R_{plasma}$ increases in time in both cases, but the increase in $R_{plasma}$ is faster in 13 mm gap than in 0.5 mm gap. Thus, the average plasma resistance is higher in 13 mm gap as well.
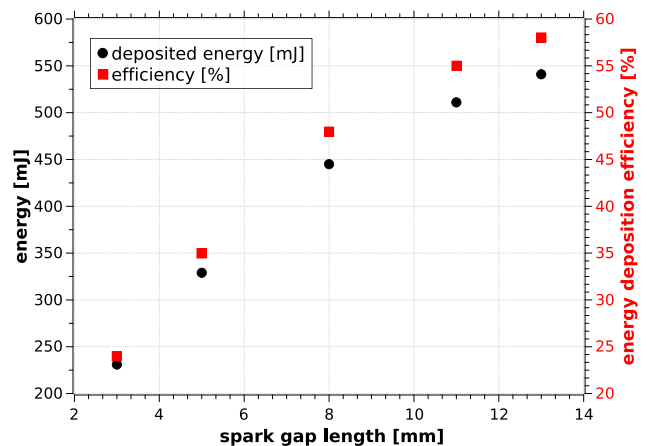


**FIG. 5.** Time evolution of $Q_{ign}$ and $Q_{el}$ during the second current pulse, calculated for gaps 3 mm (dashed lines) and 13 mm (solid lines).



**FIG. 6.** Dependence of $Q_{ign}(\infty)$ and $\eta_{ign}$ on spark gap size.

Figure 8 shows minimal and average values of the plasma resistance as functions of the gap size. Both the minimal and the average plasma resistance confirm general trend of the increasing plasma resistance with growing gap size. At 0.5 mm, $R_{plasma}$ is actually too small, and our calculation method leads to a negative value in the case of several data points shown in Fig. 7. Therefore, we could not calculate $Q_{ign}$ with sufficient accuracy for the gap 0.5 mm (the first data point on Fig. 6 is for the gap 3 mm). At 0.5 mm, major part of the available energy is deposited to the sputtering of electrodes. Rather than for ignition of combustible mixtures, our device with a gap of 0.5 mm could be useful for the production of metallic nanoparticles.

## C. Optical diagnostic of the generated plasma

Measurements of the electrical parameters prove pulsed character of the studied discharge. It is, therefore, necessary to use time-resolved optical diagnostic techniques to determine the evolution of the generated plasma characteristics. However, we first measured time-integrated spectra with the compact spectrometer to get overview of all emission lines and systems. Next, we applied the time-resolved optical emission spectroscopic technique to measure selected spectral regions.

Figure 9 shows time-integrated spectrum of plasma generated by studied high-energy system, with a gap size of 3 mm. We identified strong emission lines of Al, Cu, H, N, O, $Al^+$, and $Cu^+$. There are also weak emission lines of $N^+$ and $O^+$. There are no molecular emission systems visible in the time-integrated spectra. However, the time-resolved measurements by the iCCD camera with the adjustment of the gain enabled us to detect weak molecular nitrogen emission generated between the two current pulse. With the second current pulse onset, the atomic and ionic lines dominate even in time-resolved spectra, and molecular emission systems are not detectable. These findings may indicate strong degree of atomization and intense sputtering of electrodes during the second current pulse.

The spectrally resolved measurements show us also that the emission intensity profiles of lines of various species are different. There
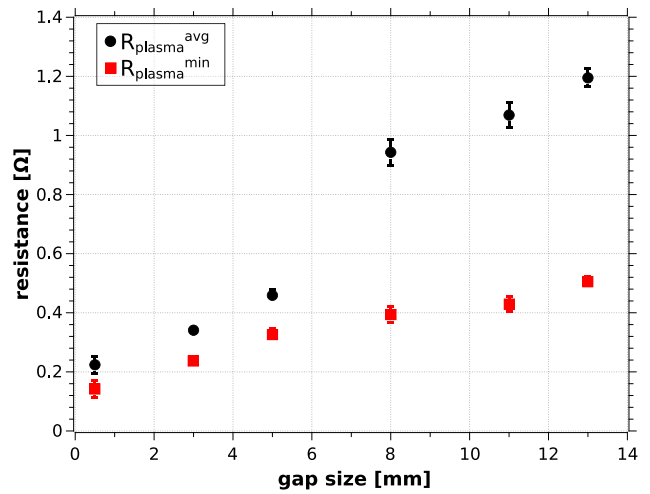


**FIG. 8.** Dependence of minimal and average values of the plasma resistance on spark gap size.

are four types of emission intensity profiles corresponding to four different types of species: (1) atomic ions of the gas origin ($N^+$ and $O^+$); (2) ions originating from the electrodes ($Al^+$ and $Cu^+$); (3) neutral atoms of gas origin (N, O, and H); (4) neutral atoms originating from the electrodes (Al and Cu).

Figure 10 shows normalized intensity profiles of four selected atomic and ionic emission lines, each representing one of the group mentioned in the previous paragraph. Each emission intensity profile reaches the peak value in more or less the same moment ($t_{max} \approx 100$ $\mu$s), but the following evolution is different. In the case of atoms and ions of gas origin (groups 1 and 3), the decrease in the emission intensity $I(t)$ can be approximated by a simple exponential decay of the first order, with a single characteristic time constant $\tau_1$,

$$I(t, t > t_{\max}) = I(t_{\max}) \times \exp\left(-(t - t_{\max})/\tau_1\right). \quad (9)$$
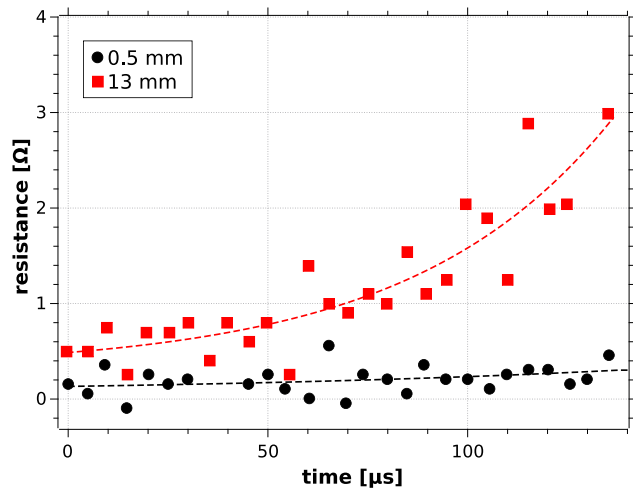


**FIG. 7.** Time evolution of the plasma resistance, calculated for two different spark gap lengths (time 0 corresponds to the $t = 1/4T$, when current during the second pulse reaches maximum).
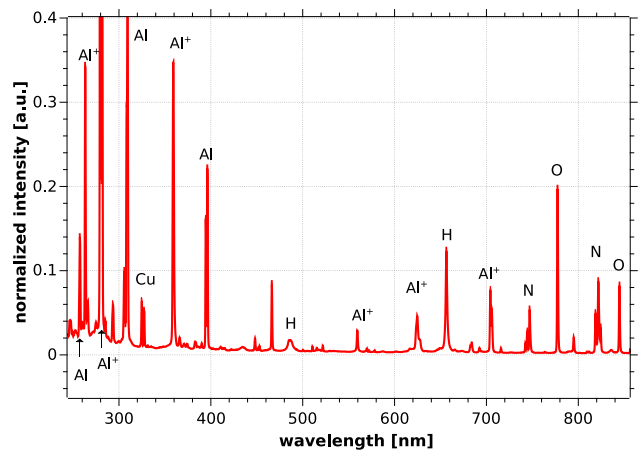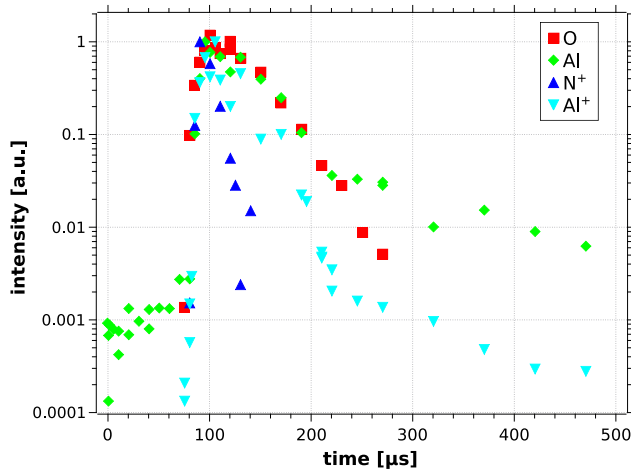


**FIG. 9.** Time-integrated optical emission spectrum of generated plasma, with a gap size of 3 mm.

**FIG. 10.** Normalized intensity profiles of four selected atomic and ionic emission lines: O triplet near 777 nm, Al at 396.15 nm, N$^+$ at 500.148 nm, and Al$^+$ at 358.692 nm.

The emission intensity profiles of the atoms and ions originating from the electrodes are more complicated. It can be approximated by the exponential decay of the second order, with two different time constants $\tau_1$ and $\tau_2$,

$$
\begin{aligned}
I(t, t > t_{\max}) = &A_1 \times \exp\left(-(t - t_{\max})/\tau_1\right) \\
&+ A_2 \times \exp\left(-(t - t_{\max})/\tau_2\right),
\end{aligned}
\tag{10}
$$

where the sum of two fitting constants $A_1$ and $A_2$ is equal to $I(t_{\max})$. The time constants $\tau_1$ and $\tau_2$ were obtained by fitting the experimental data. Details about the selected emission lines and the observed time constants are summarized in Table I.

The shortest characteristic lifetime has the emission of the N$^+$ line, with a characteristic decay time $\tau_1 = 11 \pm 2$ $\mu$s. The second fastest intensity decline is characteristic for Al$^+$ ionic line. It is worth to emphasize that after the initial relatively fast decline, $\tau_1 = 23 \pm 2$ $\mu$s, the intensity of Al$^+$ line starts to decrease much more slowly, with a characteristic decay time $\tau_2 = 125 \pm 5$ $\mu$s. Relatively weak emission of Al$^+$ can be, therefore, observed during the entire second current pulse.

The intensity of neutral lines emission declines even slower than the intensity of the Al$^+$ line. The first characteristic decay time $\tau_1$ of

**TABLE I.** Description of selected atomic and ionic emission lines. Their normalized intensity profiles are shown in Fig. 10.

| Species | $\lambda$ (nm) | Transition (s) | Group |
|---|---|---|---|
| N$^+$ | 500.148 | $^3D_2$–$^3F^o_3$ | 1 |
| Al$^+$ | 358.692 | $^3D_3$–$^3F^o_3$ | 2 |
|  | 358.707 | $^3D_2$–$^3F^o_3$ |  |
| O | 777.194 | $^5S^o_2$–$^5P_3$ | 3 |
|  | 777.417 | $^5S^o_2$–$^5P_2$ |  |
|  | 777.539 | $^5S^o_2$–$^5P_1$ |  |
| Al | 396.150 | $^2P^o_{3/2}$–$^2S_{1/2}$ | 4 |

both O and Al lines on Fig. 10 is around $30 \pm 3$ $\mu$s. The profiles of N and Al emission lines start to differ in time 220 $\mu$s. The Al line intensity decreases much slower afterward, with a characteristic decay time $\tau_2 = 140 \pm 5$ $\mu$s. Thus, the emission lines of the excited Al species are visible even after the end of the second current pulse, when the discharge current is already not measurable by our devices.

Long duration and high intensity of Al and Al$^+$ emission lines show that the sputtering of electrodes significantly influences the lifetime of the generated plasma after the second current pulse. However, the sputtering was not critical, and we had to adjust the gap size only after several hours of measurements. Moreover, alumina is not typically used at the spark plugs, and we will not use it in future during experiments focused on ignition reliability. More interesting is the high intensity and relatively long duration of O and H lines emission. Chemically active components, such as atomic oxygen and hydrogen, generated efficiently during the second current pulse can promote the activation of the chemical reactions during the combustion initiation process.

### 1. Temperature evolution in generated plasma

Spark discharge is commonly considered to generate thermal plasma, where the energy of neutrals, ions, and electrons can be characterized by the same temperature. In our system, however, it is not possible to claim that the thermodynamic equilibrium exists all the time because of the pulsed character of the discharge. Thus, it is worth to study the temperature evolution of different species, electrons, ions, and neutrals in our plasma. The temperature of neutrals in atmospheric pressure air plasmas can be approximated by rotational temperature $T_r$ of N$_2$(C$^3\Pi_u$) species,[18] obtained by fitting of the molecular nitrogen second positive emission system, N$_2$ SPS.

The rotational temperature of N$_2$(C$^3\Pi_u$) can be obtained by fitting the experimental N$_2$ SPS spectra. For this purpose, we used synthetic spectra generated by the software Specair.[18,26] The temperature of electrons can be approximated by the electron excitation temperature obtained by fitting of emission spectra of several atomic or ionic lines. For this purpose, we used our own program.

Although there is no molecular nitrogen emission visible in the time-integrated spectrum (Fig. 9), the spectrally resolved measurements reveal the presence of N$_2$ SPS emission during the phase between the two current pulses. Figure 11 shows an experimental spectrum of the region between 332 and 338 nm, time window $66 \pm 5$ $\mu$s from the beginning of the first current pulse. Shown spectrum is formed by the superposition of two emission systems: NH(A-X) and N$_2$ SPS (transition between vibrational levels 0 and 0). Measured spectrum is fitted by synthetic emission spectra of N$_2$ SPS and NH(A-X) generated by Specair for rotational and vibrational temperature 6500 K.

In later phase, delay >80 $\mu$s, the N$_2$ SPS spectra are already too weak and noisy to estimate the rotational temperature of N$_2$(C$^3\Pi_u$) species. Moreover, with the second current pulse onset, several strong emission lines appear in the spectra in the range 330–340 nm, dominating over N$_2$ SPS band. For this reason, it was impossible to follow further evolution of the rotational temperature by fitting the experimental spectra with the synthetic N$_2$ SPS spectra.

During the second current pulse, we focused on fitting of atomic and ionic emission spectra to estimate electron excitation temperature,
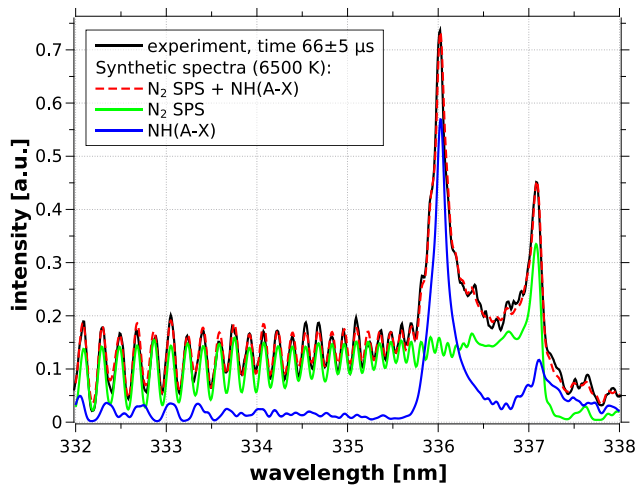
**FIG. 11.** Fitting of experimental spectrum with synthetic spectra of NH(A-X) emission system and $N_2$ second positive emission system, vibrational transition 0-0.



**FIG. 13.** Temperature evolution in generated plasma, $N_2(C^3\Pi_u)$ rotational temperature $T_r$ obtained by fitting $N_2$ SPS spectra, the excitation temperature $T_{exc}$ estimated by fitting spectra of Cu, N, and $N^+$.

$T_{exc}$. Unfortunately, the time-resolved spectra recorded by the iCCD camera cover only relatively narrow spectral region ($\sim$10 nm) where we could see only several emission lines. Moreover, these narrow spectral regions must contain at least two emission lines of the same species corresponding to radiative deexcitation from significantly different energy levels to be suitable for $T_{exc}$ estimation. Altogether, the measured spectra enabled us to estimate $T_{exc}$ from emission lines of three species: Cu, N, and $N^+$. As, for example, Fig. 12 shows time-resolved experimental emission spectrum of the spectral region 499–505 nm with several $N^+$ lines, fitted by synthetic spectra calculated for different excitation temperatures.

Figure 13 shows the evolution of $T_r$ obtained by fitting $N_2$ SPS spectra, and $T_{exc}$ estimated by fitting emission spectra of Cu, N, and $N^+$, measured with different delay relative to the appearance of the
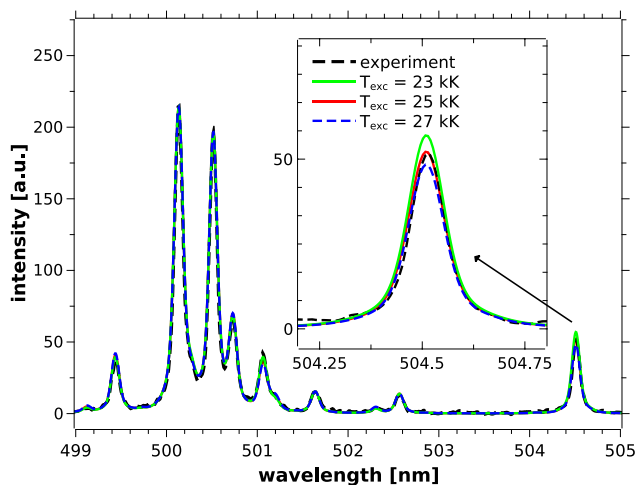


**FIG. 12.** Time-resolved emission spectra of the spectral region 499–505 nm with several $N^+$ lines, fitted by synthetic spectra calculated for different excitation temperatures, delay 100 $\mu$s, exposure time 100 ns.
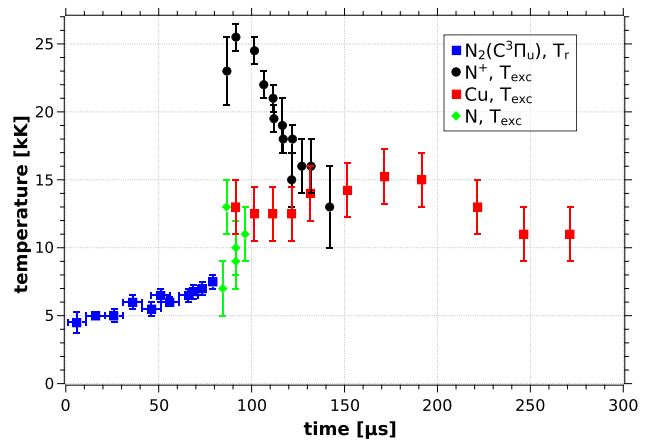
first current pulse. The exposure time used to measure these $N_2$ SPS spectra was quite long, 1–10 $\mu$s. This may be the reason why even the first value of the rotational temperature (delay 1 $\mu$s, exposure time 10 $\mu$s) is already quite high, around 4500 K. Later, the rotational temperature further increases up to around 7500 K. The uncertainty is quite high, mostly due to weak signal and overlap of $N_2$ second positive system with NH(A-X) emission system (main band at around 336 nm).

$T_{exc}$ was estimated from emission lines of three different species, but the lines around $\sim$820 nm used to estimate excitation temperature characterizing N species are very weak for time above $\sim$100 $\mu$s, and the intensity of the $N^+$ line at 504.5 nm was high enough only for time delay below $\sim$150 $\mu$s. Despite these limitations, we see that the excitation temperature of $N^+$ ions is higher than the electronic excitation temperature of neutral species at the beginning of the second current pulse (time around 100 $\mu$s on Fig. 13). However, the excitation temperature of ions decreases to around 15 kK until it equals the excitation temperature of Cu species (time 140 $\mu$s on Fig. 13). Later, the excitation temperature of Cu species slightly decreases to around 10 kK (time $>$190 $\mu$s on Fig. 13).

The fact that the obtained excitation temperature derived from N, Cu, and $N^+$ spectra differs implies that plasma is out of thermodynamic equilibrium conditions, and the temperature of free electrons probably differs from the temperature of heavy particles (for time $<$140 $\mu$s). Moreover, the population of excited levels probably does not follow the Boltzmann law.

We assume that the excitation temperature obtained by fitting of $N^+$ emission spectra is higher because the $N^+$ species emitting photons with the wavelength of 504.5 nm are excited by impact with high-energy electrons. This line is visible only when the density and the temperature of electrons are high enough. For this reason, the emission of these species fades out quickly after the peak electron density is achieved, with a characteristic decay time $\tau_1 = 11 \pm 2\,\mu$s (time $\sim$100–120 $\mu$s on Fig. 10).

The Cu emission lines around 327 nm correspond to transition to the ground state. The energy of the upper level is around 3 eV. Thus, the excited Cu species could be generated by collisions of Cu in the ground state with other heavy particles in gas having mean kinetic

energy around 1 eV ($\sim$10 kK). The Cu excitation temperature is, thus, probably in equilibrium with the kinetic temperature (energy) of heavy particles.

### 2. Electron density evolution

Figure 14 shows normalized spectrum of the region 652–660 nm with a H$\alpha$ line. The H$\alpha$ line is significantly broader compared to the line in synthetic spectrum, where the Stark effect was not taken into account, just the instrumental and Doppler broadening effects. This spectrum demonstrates that the Stark broadening effect is so significant that it is the major broadening mechanism influencing the measured line profile. Thus, it can be used to calculate the electron density in generated plasma. We used a method presented by Gigosos et al.,[25] using the full width of the half area of the H$\alpha$ line.

Figure 15 shows example spectra of spectral region 775–780 nm with the O triplet line near 777 nm. From this triplet, the intensity profile of O was derived, and a few spectra were fitted by the Specair software to estimate the electron density from the Stark broadening of these lines (see Ref. 37 for details). Figure 15 shows two experimental spectra demonstrating changes of shape of O triplet line. At delay 270 $\mu$s, the Stark broadening is already weak, and we can see three separated lines, while at delay 90 $\mu$s, the overlapping of these lines is obvious.

After analyzing a set of H$\alpha$ line and O triplet line spectra recorded at different delays, we obtained time evolution of electron density during the second current pulse (Fig. 16). The electron density during the second current pulse is high, above $10^{17}$ cm$^{-3}$, and it gradually decreases in time, from the peak value around $3\times10^{17}$ cm$^{-3}$. There is reasonable agreement between the electron density obtained from broadening of H$\alpha$ line and O triplet line. The Stark broadening mechanism of O triplet line depends also on electron temperature (we used 10 kK), not only by electron density. Moreover, the shape of line calculated by the Specair software depends also on selected gas temperature and pressure (we used 8 kK and 2 atm). If we tune the values of the gas pressure, gas temperature, and the electron temperature, we
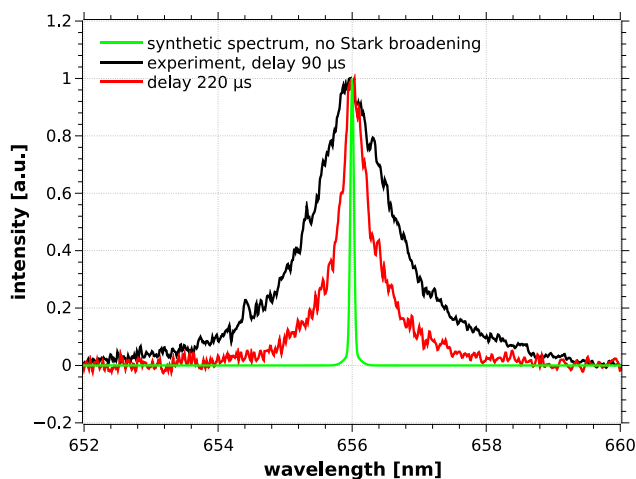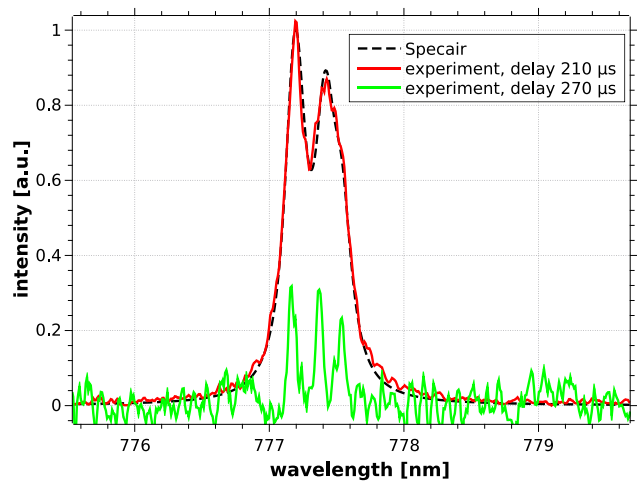


**FIG. 15.** Comparison of synthetic spectrum (calculated by Specair) with experimental spectra (O triplet near 777 nm) for delay 90 $\mu$s. The synthetic spectrum was calculated for pressure 2 atm, gas temperature 8 kK, electron temperature 10 kK, and electron density $2.16 \times 10^{17}$ cm$^{-3}$.

could, thus, achieve perfect agreement with the electron densities obtained from H$\alpha$ line.

### 3. Plasma channel diameter evolution

Finally, we used the iCCD camera in image mode to measure the evolution of the plasma channel diameter. The spectrometer's entrance slit was fully opened (300 $\mu$m), and the camera recorded 2D images of the spatial intensity distribution of spectrally unresolved light emitted by the plasma (see Fig. 17, background layer). The plasma channel image was projected perpendicularly onto the entrance slit of the spectrometer by a single convex lens. The zoom factor was 1.6. Each pixel on camera, thus, represents approximately 8.15 $\mu$m. In order to estimate the plasma channel diameter, we used intensity profile in row of illuminated pixels parallel to entrance slit (Fig. 17, smaller inlet plot
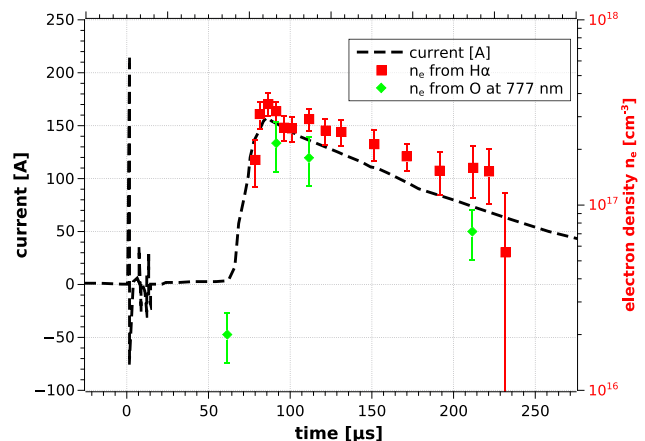


**FIG. 14.** Emission spectra of the H line at 656 nm broadened by the Stark effect, delay 90 and 220 $\mu$s. Comparison with synthetic spectrum without the Stark broadening effect.



**FIG. 16.** Evolution of electron density calculated from Stark broadening of H$\alpha$ line and obtained by fitting of O triplet near 777 nm.
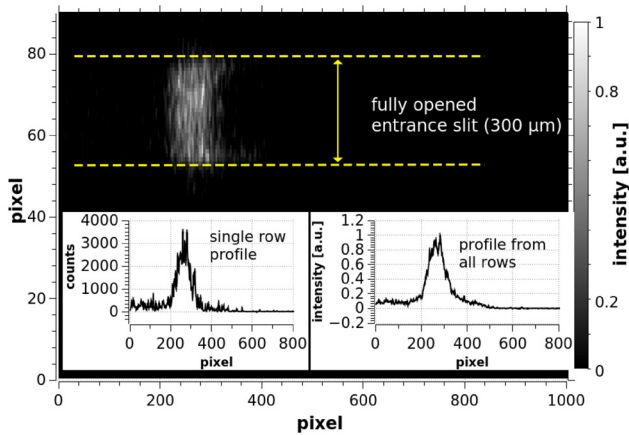
**FIG. 17.** Image of the plasma channel recorded by the iCCD camera, exposure time 250 ns and delay 90 $\mu$s; inset figures in the lower part show intensity profile from a single row of pixels (left) and normalized profile obtained as a sum of intensities from all illuminated rows (right).

down, left). In order to improve the accuracy, we have made sum of profiles from all illuminated rows (Fig. 17, smaller inlet plot down, right). The plasma channel diameter was estimated as FWHM of the final profile from sum of all illuminated rows.

Figure 18 shows the plasma channel diameter as a function of delay with respect to the beginning of the first current pulse. The diameter of the plasma channel generated by a tradition spark coil ignition systems is usually estimated on the order of 100 $\mu$m.[38] This is in a good agreement with the initial plasma diameter observed in our system right after the breakdown, 140–200 $\mu$m.

Afterward (delay 1–10 $\mu$s), the plasma channel diameter expands rapidly, at least to 3000 $\mu$m. It is not possible to guess the final value because the optical emission intensity is too weak for delay 10–50 $\mu$s. Still, we can estimate that the plasma channel diameter increases by around 3 mm in 10 $\mu$s after the first current pulse. Thus, the channel
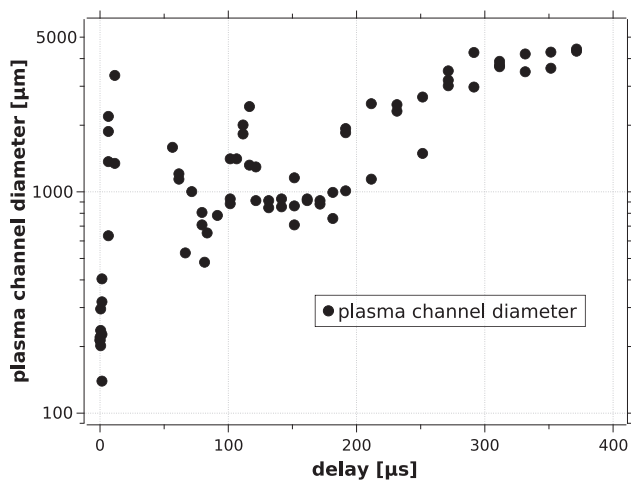


**FIG. 18.** Evolution of plasma channel diameter as a function of time from the beginning of the first current pulse.

expansion velocity is about 300 m/s, and the plasma channel diameter probably expands with sonic speed indicating shock wave formation after the first current pulse. It can be explained by the relatively fast energy deposition rate during the first current pulse. We do not know exact value of the deposited energy during the first current pulse, but we estimated that the upper limit for theoretically available energy is 163 mJ (see Subsec. III B). Assuming 10% conversion efficiency of the energy released during the discharging of $C_1$ on the primary winding of the transformer into the energy released in the spark gap, we obtain approximately 16 mJ deposited to the gap during the initial spark current pulse with a duration of 0.3 $\mu$s (Fig. 3). Thus, the average energy deposition rate is around $5 \times 10^4$ J/s.

As was already mentioned, the optical emission intensity is too weak for delay 10–50 $\mu$s. Despite this, we can deduce that the channel diameter shrinks before the onset of the second current pulse, from at least 3 mm down to around 500 $\mu$m. Meanwhile, the current in the circuit increases to about $3 \pm 1$ A. Similar behavior with a current growth enabled by the plasma channel contraction was observed in a short and weak sparks (amplitude $\sim$2 A, duration below 1 $\mu$s) in nitrogen.[39]

Despite this similarity, here, we observe specific behavior, with extremely slow current increase and plasma diameter contraction in a strong electric field between the two current pulses (delay $\sim$10–80 $\mu$s). The estimated electric field is around 2700 V/cm (voltage 800 V across 3 mm gap), and the reduced electric field strength at 300 K would be only around 11 Td (1 Td = $10^{-17}$ V cm$^2$), far below the breakdown threshold ($\sim$120 Td). However, here, the temperature increases from around 4500 K to 7500 K between two pulses (Fig. 13). If the gas pressure in the plasma channel is equal to 1 atm, the reduced electric field strength increases from $\sim$165 Td up to $\sim$270 Td between two current pulses. Thus, the reduced electric field strength would be above the breakdown threshold all the time between the two current pulses. Fast discharging of the capacitor $C_2$ and the formation of the second current pulse are inhibited by characteristics of our circuit—high reactance of the secondary winding of the transformer before the saturation of its core.

With the appearance of the second current pulse, there is steep increase in $D_p$ (delay 90–110 $\mu$s), followed by even faster decrease (delay 110–120 $\mu$s). Gradual increase in $D_p$ follows in the later phase. It is necessary to emphasize that it would require further study of the plasma channel evolution to be sure that observed evolution is really relevant. For example, it would be useful to record spectrally resolved images of the plasma channel, showing radiation from selected species only (for example, N$^+$ or Al$^+$ ions). This could help us to explain plasma diameter increase and decrease during period with delay 90–120 $\mu$s.

Despite this lack of complete explanation for plasma channel behavior, obtained results are very useful. It is known that for successful ignition, the spark kernel or hot bubble of gas created by the spark must grow to a critical size,[40] and here, we see significant increase in the final plasma diameter to almost 4 mm. Next, obtained plasma diameter allows us to estimate the specific energy deposited to gas. Assuming maximum plasma channel diameter $D_p$ = 4 mm, spark gap 3 mm, and the total deposited energy 230 mJ, the specific energy is around 3 mJ/mm$^3$.

Already the first current pulse generates the high-temperature plasma region (Fig. 13) that can cause the combustion initiation, but its lifetime does not exceed a few microseconds, and it cannot be used

for a reliable ignition due to chemical reactions delays. The second current pulse can be considered as thermal source for the reliable ignition, thanks to longer time of the thermal action exceeding 200 $\mu$s (Fig. 13) and increased size of the plasma channel diameter to 4–5 mm.

Finally, obtained plasma diameter evolution brings another possible explanation for high-energy efficiency of our ignition system. The plasma channel diameter increases by around 2.5 mm during the initial 100 $\mu$s of the second current pulse, when the major part of the energy is deposited to the gap (Fig. 6). Thus, the average channel expansion velocity is about 25 m/s, i.e., the plasma channel diameter expands with a slow subsonic speed. It can be explained by the relatively slow energy deposition rate. Approximately 180 mJ is deposited to the gap during the initial 100 $\mu$s of the second current pulse according to our calculations (Fig. 6). The average energy deposition rate during this phase is around $1.8 \times 10^3$ J/s, i.e., almost 30 times lower as estimated energy deposition rate during the first current pulse. We, therefore, assume that the shock wave is not formed during the second current pulse, and only a small fraction of the deposited energy is accumulated in the kinetic energy of gas flow. This is one of the reasons why we can achieve energy-efficient ignition in our system. At the same time, it means that the presented system is more suitable for the deflagration ignition process than for detonation.

## IV. CONCLUSIONS

Despite necessary environmental protection and switch to renewable energies, different types of internal combustion engines will be used for at least several decades. An improvement of the overall environmental performance of an engine can be achieved by feeding it with a lean mixture. However, it is difficult to ignite lean mixtures energy-efficiently. It is, therefore, desirable to develop new advanced ignition systems for reliable energy-efficient ignition of lean mixtures.

Here, we present the high-energy self-stabilized spark ignition system. Energy release and plasma characteristics were determined measuring electrical signals and optical emission spectra. There are two high current pulses. The first spark current pulse appears as a consequence of the high-voltage pulse (about 20 kV) supplied to the spark gap. The discharge current after the first current pulse gradually increases up to $3 \pm 1$ A, when the second current pulse appears. The delay between two current pulses increases with the growing spark gap size from 60 to 125 $\mu$s, corresponding to gap size of 0.5 and 13 mm, respectively. The duration of the second current pulse is about 150–300 $\mu$s, with the current amplitude of 140–180 A. The second current pulse is formed, thanks to specific features of used electrical circuit.

The deposited energy in the presented ignition system increases from 0.23 to 0.54 J as the spark gap increases from 3 to 13 mm. Interestingly, the energy efficiency of the designed system increases with increasing spark gap from 23% to 58%. The efficiency of the presented system is, therefore, much higher than the efficiency of a typical automotive ignition system.

The analysis of the optical emission spectra allowed us to evaluate the gas temperature, electron density, and the spark kernel size. These data can be used as an input for computer simulations of the ignition process during the second current pulse, when the flame kernel expansion is dominated by diffusive processes and chemical reactions. Based on obtained results, reliable ignition of the lean mixtures in high-turbulent gas flow by studied ignition system is expected. The experimental research of the combustible gas ignition by the presented system will be done in the near future.

## AUTHOR DECLARATIONS

### Conflict of Interest

The authors have no conflicts to disclose.

### Author Contributions

**Mario Janda:** Conceptualization (equal); Data curation (lead); Formal analysis (equal); Funding acquisition (equal); Investigation (equal); Methodology (equal); Project administration (equal); Software (supporting); Validation (equal); Visualization (lead); Writing – original draft (lead). **Kostyantyn Korytchenko:** Conceptualization (equal); Investigation (equal); Methodology (equal); Software (equal); Validation (equal); Writing – original draft (supporting); Writing – review & editing (lead). **Olga Shypul:** Formal analysis (equal); Software (equal); Writing – review & editing (supporting). **Serhiy Krivosheev:** Investigation (equal); Resources (lead). **Oleksandr Yeresko:** Investigation (equal). **Anatoly Kasimov:** Methodology (equal).

## DATA AVAILABILITY

The data that support the findings of this study are available from the corresponding author upon reasonable request.

## REFERENCES

[1] N. Puač, M. Gherardi, and M. Shiratani, Plasma Processes Polym. **15**, 1700174 (2018).

[2] A. Stancampiano, T. Gallingani, M. Gherardi, Z. Machala, P. Maguire, V. Colombo, J.-M. Pouvesle, and E. Robert, Appl. Sci. **9**, 3861 (2019).

[3] I. Adamovich, S. Agarwal, E. Ahedo, L. L. Alves, S. Baalrud, N. Babaeva, A. Bogaerts, A. Bourdon, P. J. Bruggeman, C. Canal, E. H. Choi, S. Coulombe, Z. Donko, D. B. Graves, S. Hamaguchi, D. Hegemann, M. Hori, H.-H. Kim, G. M. W. Kroesen, M. J. Kushner, A. Laricchiuta, X. Li, T. E. Magin, S. M. Thagard, V. Miller, A. B. Murphy, G. S. Oehrlein, N. Puac, R. M. Sankaran, S. Samukawa, M. Shiratani, M. Simek, N. Tarasenko, K. Terashima, E. Thomas, Jr., J. Trieschmann, S. Tsikata, M. M. Turner, I. J. van der Walt, M. C. M. van de Sanden, and T. von Woedtke, J. Phys. D: Appl. Phys. **55**, 373001 (2022).

[4] A. Kanzawa, Plasma Sources Sci. Technol. **2**, 58 (1993).

[5] L. Bromberg, D. Cohn, A. Rabinovich, and N. Alexeev, Int. J. Hydrogen Energy **24**, 1131 (1999).

[6] A. Kobayashi, K. Osaki, and C. Yamabe, Vacuum **65**, 475 (2002).

[7] E. Hontañón, J. M. Palomares, M. Stein, X. Guo, R. Engeln, H. Nirschl, and F. E. Kruis, J. Nanopart. Res. **15**, 1957 (2013).

[8] Y. S. Najjar, Open Fuels Energy Sci. J. **2**, 1 (2009).

[9] N. Khanal, McNair Scholars Res. J. **1**, 6 (2014).

[10] D. E. Winterbone, in *Advanced Thermodynamics for Engineers*, edited by D. E. Winterbone (Butterworth-Heinemann, Oxford, 1997), pp. 291–315.

[11] M. Girard and G. Gaborel, European patent EP3051101A1 (3 August 2016).

[12] D. Ballal and A. Lefebvre, Proc. R. Soc. London, Ser. A **357**, 163 (1977).

[13] G. J. Rohwein and L. S. Camilli, in *SAE Powertrain & Fluid Systems Conference and Exhibition* (SAE International, 2002).

[14] H. Shimojo and T. Inamura, US patent 4136301A (23 January 1979).

[15] P. J. Porreca and E. A. VanDuyne, US patent 5197448 (30 March 1993).

[16] D. Samoilenko, A. Połaniecki, K. Szost, K. Korytchenko, R. Tomashevskiy, and O. Pedasiuk, in *2020 IEEE 4th International Conference on Intelligent Energy and Power Systems (IEPS)* (IEEE, 2020), pp. 313–316.

[17] K. V. Korytchenko, A. M. Kasimov, V. I. Golota, S. Ajmani, D. P. Dubinin, and R. G. Meleshchenko, Probl. At. Sci. Technol. **118**, 225 (2018).

[18] C. Laux, T. Spence, C. Kruger, and R. Zare, Plasma Sources Sci. Technol. **12**, 125 (2003).

[19] U. Fantz, Plasma Sources Sci. Technol. **15**, S137–S147 (2006).

[20] D. Lacoste, D. Xu, J. Moeck, and C. Laux, Proc. Combust. Inst. **34**, 3259 (2013).

[21] F. Tholin, D. A. Lacoste, and A. Bourdon, Combust. Flame **161**, 1235 (2014).

[22] N. Konjević, A. Lesage, J. Fuhr, and W. Wiese, J. Phys. Chem. Ref. Data **31**, 819 (2002).

[23] A. Lesage, New Astron. Rev. **52**, 471 (2009).

[24] N.I. of Standards and Technology, 2023.

[25] M. Gigosos, M. Gonzalez, and V. Cardenoso, Spectrochim. Acta, Part B **58**, 1489 (2003).

[26] C. Laux, *Radiation and Nonequilibrium Collisional-Radiative Models* (von Karman Institute, Rhode-Saint-Genèse, Belgium, 2002).

[27] J. Meek, Phys. Rev. **57**, 722 (1940).

[28] H. Raether, *Electron Avalanches and Breakdown in Gases* (Butterworths, London, 1964).

[29] L. Loeb, *Electrical Coronas* (University of California Press, Berkeley, 1965).

[30] Y. S. Akishev, G. I. Aponin, M. E. Grushin, V. B. Karal'nik, M. V. Pan'kin, A. V. Petryakov, and N. I. Trushkin, Plasma Phys. Rep. **34**, 312 (2008).

[31] M. Janda, Z. Machala, A. Niklová, and V. Martišovitš, Plasma Sources Sci. Technol. **21**, 045006 (2012).

[32] L. S. Camilli, J. E. Gonnella, and T. J. Jacobs, SAE Technical Paper No. 2012-01-1151 (2012).

[33] K. Korytchenko, O. Shypul, D. Samoilenko, I. Varshamova, A. Lisniak, S. Harbuz, and K. Ostapov, Electr. Eng. Electromech. **2021**, 35 (2021).

[34] Y. P. Raizer, *Gas Discharge Physics* (Springer, Berlin, Heidelberg, 2011).

[35] C. Huang, S. Shy, C. Liu, and Y. Yan, Proc. Combust. Inst. **31**, 1401 (2007).

[36] H. G. Adelman, Symp. (Int.) Combust. **18**, 1333 (1981).

[37] M. Janda, V. Martisovits, K. Hensel, L. Dvonc, and Z. Machala, Plasma Sources Sci. Technol. **23**, 065016 (2014).

[38] A. Zhang, R. Scarcelli, T. Wallner, S.-Y. Lee, and J. Naber, in *SAE 2016 World Congress and Exhibition* (SAE International, 2016).

[39] Y. S. Akishev, G. I. Aponin, M. E. Grushin, V. B. Karal'nik, A. E. Monich, M. V. Pan'kin, and N. I. Trushkin, Plasma Phys. Rep. **33**, 584 (2007).

[40] H. G. Adelman, "A time-dependent theory of spark ignition," Ph.D. thesis (University of Connecticut, 1979).